Dynamical Adjustment of Mesoscale Convective Anvils

SCOTT R. FULTON

Department of Mathematics and Computer Science, Clarkson University, Potsdam, New York

WAYNE H. SCHUBERT AND SCOTT A. HAUSMAN

Department of Atmospheric Science, Colorado State University, Fort Collins, Colorado

(Manuscript received 27 June 1994, in final form 28 March 1995)

ABSTRACT

Observational evidence indicates that upper-tropospheric and lower-stratospheric anticyclones occur in mesoscale convective systems, possibly resulting from the vertical redistribution of mass. The authors examine the gradient adjustment process that occurs when mass from the lower troposphere is impulsively injected between isentropic levels in the vicinity of the tropopause. Formulating the quasi-static primitive equations for inviscid, adiabatic, axisymmetric flow on an f plane using entropy and potential radius coordinates allows us to compute the final state in gradient balance by solving a single nonlinear elliptic problem. Solutions of this elliptic problem illustrate the development of an anticyclonic lens at the level of mass injection, with accompanying cold and warm temperature anomalies above and below, respectively. For a given amount of injected mass, a lower-stratospheric injection results in a stronger anticyclone than does an upper-tropospheric injection. Mass injections at low latitudes result in anticyclonic lens structures that are of larger horizontal extent and smaller vertical extent. The entrainment of stratospheric air into the mesoscale convective anvil is also shown to have an effect on the structure of the anticyclone. The theoretical results presented here are in substantial agreement with recent observations of the structure of upper-level anticyclones produced by mesoscale convective systems.

1. Introduction

In the intense cumulonimbus convection that occurs in midlatitude and tropical mesoscale convective systems, undilute updrafts often inject large amounts of mass into isentropic layers that straddle the tropopause. Several examples of the upper-tropospheric and lower-stratospheric effects produced by such mesoscale convective systems were discussed by Fritsch and Maddox (1981a,b), who presented 200-mb maps of the vector difference between the observed flow (after the development of a convective system) and the predicted flow from a numerical weather prediction model capable of simulating flow evolution without the influence of organized, penetrative convection. Such vector difference maps isolate the upper-tropospheric effects of mesoscale convection. One of Fritsch and Maddox's 200-mb vector difference maps is shown in Fig. 1. At this time, digitized infrared satellite data showed a region of cold cloud tops over eastern Iowa, northern Missouri, and western Illinois. Surrounding this region is a strong anticyclonic anomaly with approximately 20 m s^{-1} winds.

Corresponding author address: Dr. Scott R. Fulton, Dept. of Mathematics and Computer Science, Clarkson University, Box 5815, Potsdam, NY 13699-5815.

A second example from Fritsch and Maddox (1981a) contains additional information on the temperature field and is shown in Fig. 2. Again, there is a distinct anticyclone at 200 mb, as shown in Fig. 2a. This figure is the result of a scale-separation analysis (Maddox et al. 1981) designed to isolate the mesoscale circulation. The 300-mb temperature structure (just below the anticyclone) is shown in Fig. 2b. It consists of a warm region with temperature approximately 3.5°C higher than in the surrounding air 700 km from the anticyclone center. The 150-mb temperature structure (just above the anticyclone) is shown in Fig. 2c. In contrast to the 300-mb structure, the 150-mb pattern consists of a cold region with temperature approximately 8°C lower than in the surrounding air 700 km from the anticyclone center. Figures 1 and 2 are typical of the 10 cases studied by Fritsch and Maddox. All cases have 200-mb anticyclonic flow anomalies of 10–20 m s^{-1}.

One view of such convectively induced mesohighs in the upper troposphere and lower stratosphere is that they result from the nearly instantaneous injection of undilute lower-tropospheric air into a mesoscale convective anvil. Such an injection would cause a transient dynamical adjustment toward a steady balanced flow determined by the potential vorticity anomaly associated with the mass injection. Observational support for this view can be found in the work of Bosart and Niel-

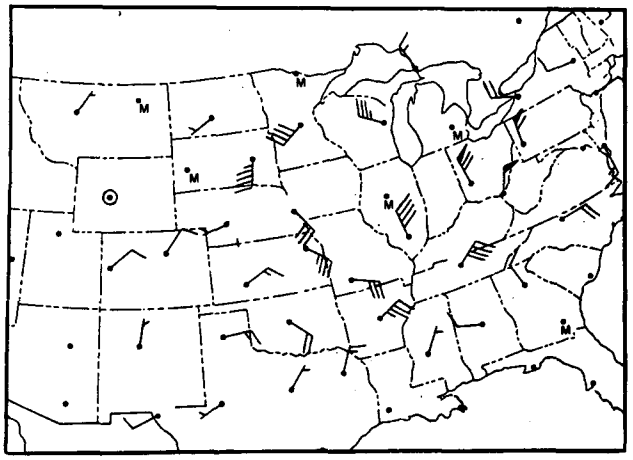

FIG. 1. Vector difference between the observed 200-mb flow and the flow predicted by a NWP model without the effects of organized, penetrative convection. At this time (1200 UTC 27 June 1979) there existed a satellite-observed cirrus cloud shield approximately 600 km in diameter centered over southeastern Iowa. Full wind barbs indicate 5 m s^{-1}, and flags 25 m s^{-1} (from Fritsch and Maddox 1981a).

sen (1993), who studied a convective cluster that occurred along the Gulf of Mexico coast on 26 April 1991. Between 0830 and 1130 UTC the convective cluster developed east of Lake Charles, Louisiana. By 1400 UTC infrared satellite imagery revealed a 600-km-diameter region of cold cirrus cloud tops. The 1200 UTC sounding (launched at approximately 1115 UTC) from Lake Charles began its ascent west of the cirrus anvil region but drifted approximately 60 km to the east during the 40 min required to reach 200 mb. The sounding then penetrated through the western edge of the growing anvil. The remarkable nature of this sounding is shown in Fig. 3. The anvil air is between 185 and 135 mb and consists of undilute air from the nearly saturated lower troposphere. Bosart and Nielsen conclude from this sounding (and the nearby soundings at Slidell and Jackson, also shown in Fig. 3) that there has been undilute ascent of boundary layer air to a level 2.6 km higher than the surrounding undisturbed tropopause.

We shall use the work of Bosart and Nielsen as the motivation and the observational basis for the gradient adjustment calculations presented here. The calculations yield the final balanced state, consistent with the nonlinear primitive equations, after an impulsive redistribution of mass. The present approach is similar in concept but different in detail to that of Shutts et al. (1988), who have used a novel Lagrangian element model (or "geometric model") to construct axisymmetric, gradient vortex states that ultimately result after element rearrangement due to penetrative convection. Their solutions show the formation of tight, low-level cyclones and broad upper-level anticyclonic lenses. Their results are also qualitatively consistent with the idealized analytic solutions obtained by Shutts (1987) for rectilinear, geostrophic flow using the conformal mapping techniques of Gill (1981).

In an effort to understand the fundamental dynamical adjustment that occurs in mesoscale convective anvils, let us consider the following problem, which is similar in spirit to those of Gill (1981), Shutts (1987), and Shutts et al. (1988). Suppose that resting upper-tropospheric and lower-stratospheric isentropic layers are impulsively disturbed by an injection of mass that locally thickens these layers. In the lower parts of the disturbed region isentropes bow downward, resulting in a localized warm region. In the upper parts of the disturbed region isentropes bow upward, resulting in a localized cold region. During adiabatic adjustment the lower warm region ascends and the upper cold region descends (Balsley et al. 1988; Johnson et al. 1990), air moves laterally outward between isentropic surfaces, and Coriolis effects produce an anticyclone. The final balanced state consists of an anticyclonic lens with a local tropopause anomaly. We can think of this as a generalized version of the classic Rossby adjustment problem. In section 2 we describe the precise mathematical formulation of this nonlinear, gradient adjustment problem in the radius coordinate. A more convenient formulation in the potential radius coordinate is described in section 3. In section 4 we present some solutions that illustrate how the structure of the anticyclone depends on the magnitude, height, and latitude of the mass injection. In section 5 we explore how the entrainment of stratospheric air by overshooting convective turrets can affect the structure of the anticyclone.

2. Gradient adjustment in the radius coordinate

We consider a compressible, stably stratified, quasi-static atmosphere on an f plane. Rather than using potential temperature θ as the vertical coordinate, we use specific entropy $s = c_p \ln(\theta/\theta_0) = c_p \ln(T/T_0) - R_d \ln(p/p_0)$, where R_d is the gas constant for dry air, the pressure p and the absolute temperature T are related to the density ρ by the ideal gas law $p = \rho R_d T$, and the subscript "0" denotes a constant reference value, with $\theta_0 = T_0$. The use of specific entropy rather than potential temperature results in a somewhat simpler hydrostatic equation, the right-hand side of which is simply the temperature rather than the Exner function. Using cylindrical coordinates in the horizontal, the quasi-static primitive equations for inviscid, adiabatic, axisymmetric flow on an f plane can be written

$$\frac{Du}{Dt} - \left(f + \frac{v}{r}\right)v + \frac{\partial M}{\partial r} = 0, \qquad (2.1)$$

$$\frac{Dv}{Dt} + \left(f + \frac{v}{r}\right)u = 0, \qquad (2.2)$$

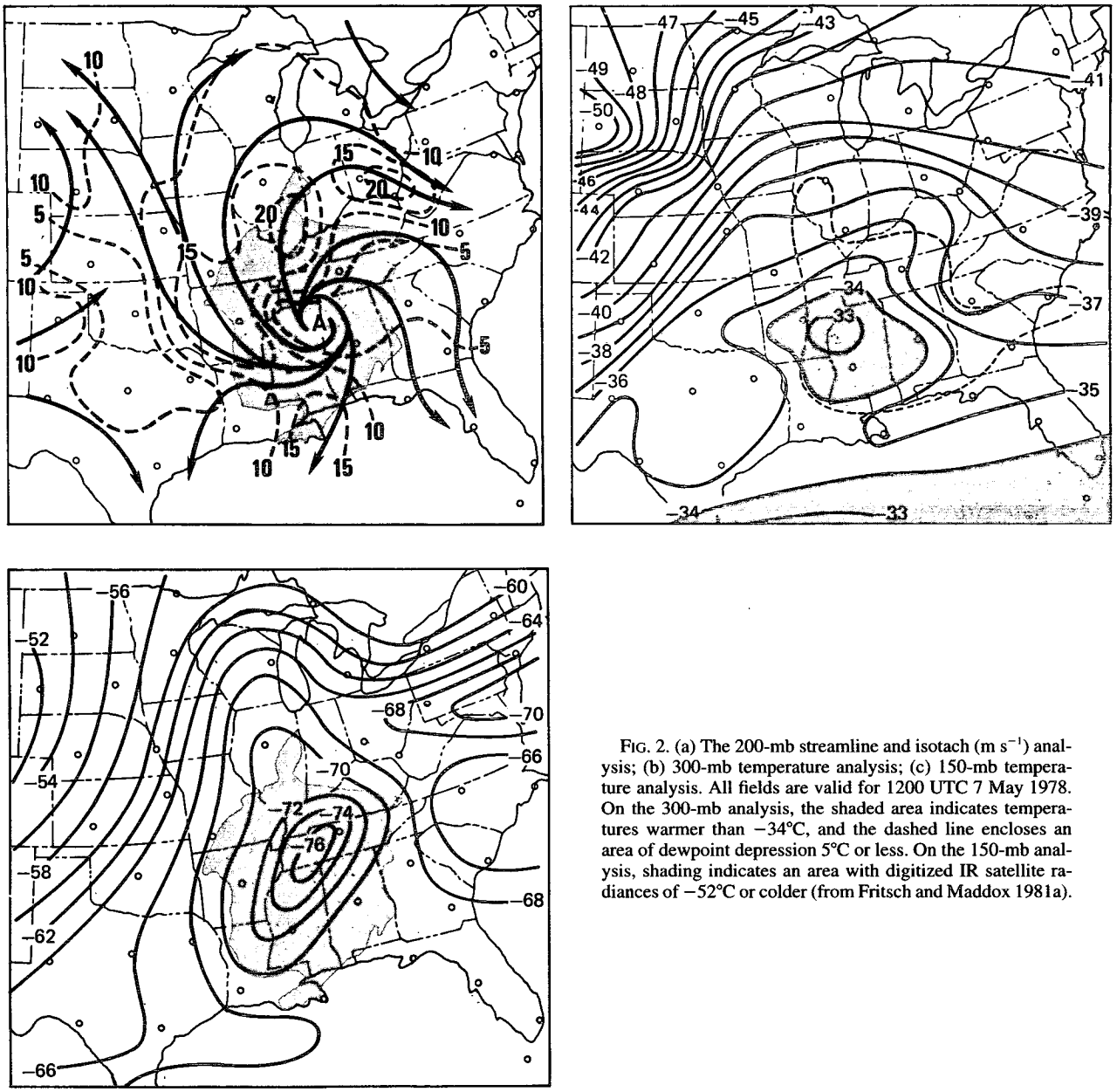

FIG. 2. (a) The 200-mb streamline and isotach (m s^{-1}) analysis; (b) 300-mb temperature analysis; (c) 150-mb temperature analysis. All fields are valid for 1200 UTC 7 May 1978. On the 300-mb analysis, the shaded area indicates temperatures warmer than −34°C, and the dashed line encloses an area of dewpoint depression 5°C or less. On the 150-mb analysis, shading indicates an area with digitized IR satellite radiances of −52°C or colder (from Fritsch and Maddox 1981a).

$$\frac{\partial M}{\partial s} = T, \tag{2.3}$$

$$\frac{D\sigma}{Dt} + \sigma \frac{\partial (ru)}{r\partial r} = 0, \tag{2.4}$$

where

$$\frac{D}{Dt} = \frac{\partial}{\partial t} + u \frac{\partial}{\partial r} \tag{2.5}$$

is the material derivative, u and v the radial and tangential components of the wind, $M = c_pT + gz$ the Montgomery potential, and $\sigma = -\partial p/\partial s$ the pseudo-density in s-space. Using the definition of σ and the relation $T = T_0 e^{s/c_p}(p/p_0)^\kappa$, the set (2.1)–(2.4) can be considered closed in the unknowns u, v, M, T, σ, and p.

If we specify an initial condition such that $u = 0$ and $(f + v/r)v \neq \partial M/\partial r$, then u will be generated through (2.1), and the rotational wind field v and the mass field σ will subsequently change through (2.2) and (2.4). As gravity–inertia waves propagate outward, the rotational flow will come into gradient adjustment, and u will return to zero. This nonlinear gradient adjustment process consists of two parts—the transient part and

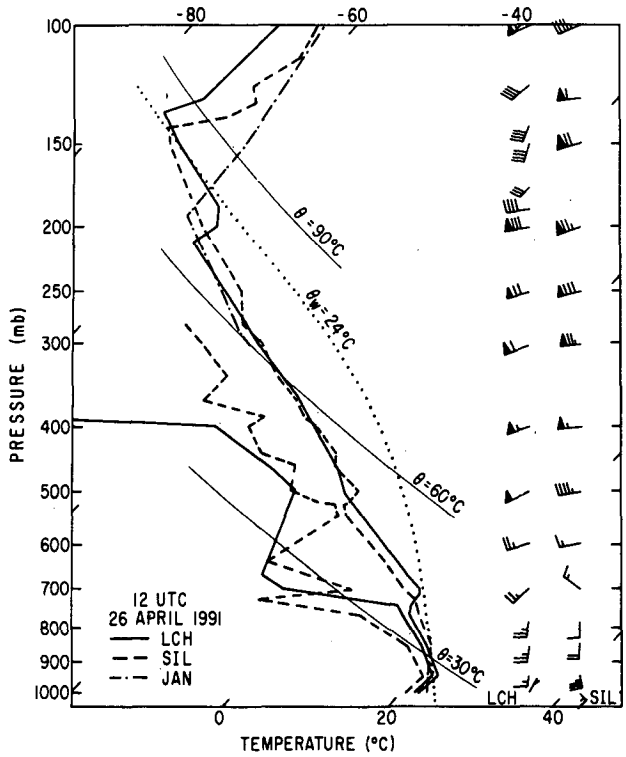

FIG. 3. Soundings at 1200 UTC 26 April 1991 for Lake Charles, Louisiana (LCH), Slidell, Louisiana (SIL), and Jackson, Mississippi (JAN). The Lake Charles sounding penetrated through a cirrus anvil between 185 and 135 mb. As shown by the 24°C wet-bulb potential temperature curve, the anvil consisted of undilute air from the nearly saturated boundary layer. The 300–100-mb portion of the Jackson temperature sounding shows a tropopause at 195 mb, which was typical of the atmosphere everywhere before convection started and typical of the environment far from convection after convection started. Note that the injection of anvil air resulted in the downward displacement of the tropopause from 195 to 215 mb (from Bosart and Nielsen 1993).

the final adjusted part. Although the transient part is complicated, its linear aspects can be treated analytically (Schubert et al. 1980; Fulton and Schubert 1980; Shutts 1994). The final adjusted part of the problem can be treated using the potential vorticity conservation principle and is independent of the details of the transient part of the adjustment. Here we shall discuss only the final adjusted state.

The potential vorticity principle associated with the set (2.1)–(2.4) can be derived by first noting that the equation for the *isentropic absolute vorticity* takes the form

$$\frac{D\zeta}{Dt} + \zeta \frac{\partial(ru)}{r\partial r} = 0, \tag{2.6}$$

where $\zeta = f + \partial(rv)/r\partial r$ is the isentropic absolute vorticity. Eliminating the isentropic divergence between (2.4) and (2.6), we obtain

$$\frac{DP}{Dt} = 0, \tag{2.7}$$

where $P = \zeta/\sigma$ is the potential vorticity.

An initially unbalanced state will have adjusted to gradient wind balance when transient gravity–inertia waves have propagated into the far field. In this balanced state, we have

$$f + \frac{\partial(rv)}{r\partial r} + P\frac{\partial p}{\partial s} = 0, \tag{2.8}$$

$$\left(f + \frac{v}{r}\right)v = \frac{\partial M}{\partial r}, \tag{2.9}$$

$$\frac{\partial M}{\partial s} = T_0 e^{s/c_p}\left(\frac{p}{p_0}\right)^{\kappa}, \tag{2.10}$$

with boundary conditions $p = p_T$ at $s = s_T$, $M = c_pT_0(p/p_0)^{\kappa}$ at $s = 0$, and $p \to \bar{p}$ as $r \to \infty$. These boundary conditions are derived using the assumptions that the upper isentropic surface ($s = s_T$) is an isobaric surface ($p = p_T$), the lower isentropic surface ($s = 0$) is a constant height surface ($z = 0$), and the pressure p approaches a specified far-field pressure $\bar{p}(s)$ as $r \to \infty$. Equations (2.8)–(2.10), along with the associated boundary conditions, constitute an invertibility principle for $v(r, s)$, $M(r, s)$, and $p(r, s)$ in terms of the potential vorticity $P(r, s)$ and the mean mass distribution $\bar{p}(s)$. In other words, given $\bar{p}(s)$, if we could use (2.7) to determine the potential vorticity of the final adjusted state as a function of (r, s), (2.8)–(2.10) could be solved for the three unknowns $v(r, s)$, $M(r, s)$, and $p(r, s)$. Alternatively, by various elimination procedures, we could also express the invertibility principle in three different ways, that is, as second-order partial differential equations for any of the variables v, M, or p. The equation for v was discussed by Hoskins et al. (1985); related papers by Thorpe (1985, 1986) discuss the invertibility principle in pressure-type coordinates. As an example of another way to look at the invertibility problem, let us consider the second-order partial differential equation for M. To express the invertibility problem in terms of M, we first multiply (2.9) by r^3, then differentiate the result with respect to r, and finally use (2.8) and (2.10) to eliminate $f + \partial(rv)/r\partial r$ and p. The result is

$$f^2 + \frac{\partial}{r^3\partial r}\left(r^3\frac{\partial M}{\partial r}\right) + c_p\rho P\left(f + \frac{2v}{r}\right) \times e^{s/c_p}\frac{\partial}{\partial s}\left(e^{-s/c_p}\frac{\partial M}{\partial s}\right) = 0, \tag{2.11a}$$

with boundary conditions

$$\frac{\partial M}{\partial s} = T \quad \text{at} \quad s = s_T, \tag{2.11b}$$

$$c_p\frac{\partial M}{\partial s} = M \quad \text{at} \quad s = 0, \tag{2.11c}$$

$$M \to \bar{M} \quad \text{as} \quad r \to \infty. \tag{2.11d}$$

Here $\bar{M}(s)$ is the far-field profile of Montgomery potential associated with $\bar{p}$.

All the above ways of looking at the adjustment problem suffer from the same complication—the determination of the final potential vorticity field as a function of (r, s). The difficulty is that (2.7) states that P is conserved on fluid particles, so that the determination of the final P field as a function of (r, s) depends on the complicated advection by the oscillating (due to gravity–inertia wave propagation) u field. One way around this nagging problem is the often-used tacit assumption that the adjustment process itself does not locally disturb the potential vorticity field. However, this assumption is not valid for the large radial shifts in fluid particle location found in the nonlinear adjustments presented here. As shown in section 3, the problem can be circumvented by transforming to a new radial coordinate that converts (2.7) into a "local" conservation equation, making u implicit in the coordinate transformation. This approach has become standard in balanced vortex studies (e.g., Shutts and Thorpe 1978; Gill 1981; Schubert and Hack 1983; Thorpe 1985, 1986; Hack and Schubert 1986; Schubert and Alworth 1987; Emanuel 1989), and here we extend it to the primitive equations. We review this approach in the following section.

3. Gradient adjustment in the potential radius coordinate

To accomplish the radial coordinate transformation, we first note that the tangential momentum equation (2.2) can also be written in the absolute angular momentum form $D(rv + 0.5fr^2)/Dt = 0$. Since absolute angular momentum is conserved, one might expect certain advantages in using it as a coordinate in place of r. We follow this general approach but, in particular, use as a new coordinate the potential radius R (Schubert and Hack 1983), which is related to the actual radius r and the tangential wind v by $0.5fR^2 = rv + 0.5fr^2$. This relation allows the potential radius to be interpreted as the radius to which an air parcel must be moved (conserving absolute angular momentum) in order for its tangential wind component to vanish. Let us now consider $(R, S, \mathcal{T})$ space, where $S = s$ and $\mathcal{T} = t$. The symbols S and $\mathcal{T}$ are introduced to distinguish partial derivatives at fixed r ($\partial/\partial s$ and $\partial/\partial t$) from partial derivatives at fixed R ($\partial/\partial S$ and $\partial/\partial \mathcal{T}$). Derivatives in (r, s, t) space are then related to derivatives in $(R, S, \mathcal{T})$ space by

$$\left(\frac{\partial}{\partial r}, \frac{\partial}{\partial s}, \frac{\partial}{\partial t}\right) = \left(\frac{\partial R}{\partial r}\frac{\partial}{\partial R}, \frac{\partial R}{\partial s}\frac{\partial}{\partial R} + \frac{\partial}{\partial S}, \frac{\partial R}{\partial t}\frac{\partial}{\partial R} + \frac{\partial}{\partial \mathcal{T}}\right). \tag{3.1}$$

Using the first and last entries of (3.1) we can now easily show that (2.5) can also be written as

$$\frac{D}{Dt} = \frac{\partial}{\partial \mathcal{T}}. \tag{3.2}$$

The advantage of (3.2) over (2.5) is the elimination of the divergent wind component u, which is now implicit in the coordinate transformation. Thus, the material conservation relation (2.7) has been converted into a local conservation relation.

Since our basic conservation principle is now expressed in (R, S) space, we must transform our invertibility principle (2.8)–(2.10) to this same space. In doing so, we shall find it convenient to use the inverse potential vorticity, that is, to use the potential pseudodensity $\sigma^* = (f/\zeta)\sigma$, which can be written in Jacobian form using

$$\sigma^* = \frac{f}{\zeta}\sigma = -\frac{\partial(0.5r^2)}{\partial(0.5R^2)}\frac{\partial p}{\partial s} = -\frac{\partial(0.5r^2, s)}{\partial(0.5R^2, S)}\frac{\partial(0.5r^2, p)}{\partial(0.5r^2, s)} = -\frac{\partial(0.5r^2, p)}{\partial(0.5R^2, S)}. \tag{3.3}$$

Expressed in terms of σ^* and using (3.2), the conservation principle (2.7) now becomes

$$\frac{\partial \sigma^*}{\partial \mathcal{T}} = 0. \tag{3.4}$$

Introducing the new dependent variable $\mathcal{M} = M + 0.5v^2$, the invertibility principle (2.8)–(2.10) in (r, s, t) space transforms to

$$\frac{\partial(0.5r^2, p)}{\partial(0.5R^2, S)} + \sigma^* = 0, \tag{3.5}$$

$$f\frac{R}{r}v = \frac{\partial \mathcal{M}}{\partial R}, \tag{3.6}$$

$$\frac{\partial \mathcal{M}}{\partial S} = T \tag{3.7}$$

in $(R, S, \mathcal{T})$ space. The advantage of (3.5)–(3.7) is that u has become implicit in the coordinate transformation. Of course, it is still possible to recover the particle shifts associated with u since solutions of the invertibility relations (3.5)–(3.7) yield $v(R, S)$ and hence $r(R, S)$. For our purposes it is convenient to combine (3.5)–(3.7) into a single equation for $\mathcal{M}$. Thus, eliminating v and p in favor of $\mathcal{M}$, we obtain

$$\left[f^2 - R^3\frac{\partial}{\partial R}\left(\frac{\partial \mathcal{M}}{R^3 \partial R}\right)\right]e^{S/c_p}\frac{\partial}{\partial S}\left(e^{-S/c_p}\frac{\partial \mathcal{M}}{\partial S}\right) + \left(\frac{\partial^2 \mathcal{M}}{\partial R \partial S}\right)^2 + \frac{\sigma^*}{\rho c_p}\left(f + \frac{2}{f}\frac{\partial \mathcal{M}}{R \partial R}\right)^2 = 0, \tag{3.8a}$$

which is the desired relation between $\mathcal{M}$ and σ^*. We take the upper boundary to be an isentropic surface with entropy S_T and specify the temperature T there (e.g., T is constant for an isothermal top), so the upper boundary condition for (3.8a) is simply

$$\frac{\partial \mathcal{M}}{\partial S} = T \quad \text{at} \quad S = S_T, \tag{3.8b}$$

where $S_T = c_p \ln(\theta_T/\theta_0)$. Likewise, we take the lower boundary to be the isentropic surface with potential temperature $\theta = \theta_0$; assuming this is flat (i.e., $z = 0$ there), we have $M = c_pT$ at $S = 0$. Written in terms of $\mathcal{M}$, this lower boundary condition becomes

$$\left(f^2 + \frac{2}{R}\frac{\partial \mathcal{M}}{\partial R}\right)\left(\mathcal{M} - c_p\frac{\partial \mathcal{M}}{\partial S}\right) - \frac{1}{2}\left(\frac{\partial \mathcal{M}}{\partial R}\right)^2 = 0 \quad \text{at} \quad S = 0. \tag{3.8c}$$

For the outer boundary condition, we wish to impose at finite R a condition that simulates an infinite domain. This can be accomplished in a variety of ways. Here, we will simply assume that an isolated potential pseudodensity anomaly is produced and choose the outer boundary $R = a$ large enough so that σ^* and $\mathcal{M}$ can be assumed to be independent of R there. Then the invertibility problem at $R = a$ can be solved as a one-dimensional problem in S. Specifically, we integrate $\sigma^* = \sigma = -\partial p/\partial S$ to obtain p and then integrate the hydrostatic equation to obtain $\mathcal{M}$ at $R = a$, thus giving specified (Dirichlet) outer boundary values for the solution of (3.8a). Finally, we note that a boundary condition is not necessary at $R = 0$. Rather, the appropriate limiting form of the invertibility relation at $R = 0$ should be used. This limiting form is derived in the appendix.

We can now summarize the results of our analysis as follows. Because of (3.4), the final σ^* field is equal to the initial field, that is, $\sigma^*(R, S, \infty) = \sigma^*(R, S, 0)$. Inserting this $\sigma^*(R, S, 0)$ into (3.8), we can then solve for $\mathcal{M}$, after which the wind field v and the mass field T can be determined from (3.6) and (3.7). This is all accomplished in (R, S) space. The transformation to other representations, for example, $v(r, s)$ or $v(r, p)$, is straightforward.

The diagnostic problem (3.8) involves nonlinearity in both the partial differential equation (3.8a) and the lower boundary condition (3.8c); also, the density ρ in (3.8a) depends nonlinearly on $\mathcal{M}$ through the hydrostatic relation and $\rho = \rho_0(T/T_0)^{(1-\kappa)/\kappa}e^{-S/R_d}$, where $\rho_0 = p_0/(R_dT_0)$. However, as is briefly discussed by Schubert and Alworth (1987), if we limit our attention to the situation where the potential pseudodensity and the absolute vorticity are positive and ρ is fixed, the solution of (3.8) is unique.

We solve the invertibility relation (3.8) by a method essentially similar to that of Schubert and Alworth (1987), discretizing the problem by second-order finite differences and solving iteratively by a simple Gauss–Seidel relaxation scheme. When the solution is only weakly nonlinear, this procedure works well and can be accelerated by multigrid processing as described by Fulton (1989). However, solving for strongly nonlinear flows is rather touchy and works best on a single grid with continuation (i.e., use the solution from a weaker case as the initial approximation for the Gauss–Seidel iteration). The transformation from (R, S) back to physical space (r, p) for displaying the solutions is accomplished by interpolating in one coordinate direction at a time using cubic Hermite splines with monotonicity preserved.

4. Examples of balanced flows produced by impulsive mass redistributions

Our initial condition consists of a resting atmosphere, so that $R = r$ initially and $\sigma^*(r, s, 0) = \sigma(r, s, 0)$, with the initial pseudodensity field given by

$$\sigma(r, s, 0) = \bar{\sigma}(s) + \sigma'(r, s), \tag{4.1}$$

where $\bar{\sigma}$ is a horizontally uniform basic state representing the atmosphere before the convection occurs and σ' is a perturbation representing the impulsive transfer of mass due to convection. For the basic state we use the $\bar{\sigma}(s)$ profile determined hydrostatically from the temperature profile shown by the dashed line in Fig. 4b. This profile has a tropopause at 200 mb. For the perturbation (representing the effects of convection) we take

$$\sigma'(r, s) = \hat{\sigma}F(r)G(s), \tag{4.2}$$

where the constant $\hat{\sigma}$ specifies the amplitude of the perturbation, $F(r)$ its horizontal profile, and $G(s)$ its vertical profile. For $F(r)$ we take

$$F(r) = \begin{cases} 1, & 0 \leq r \leq r_1, \\ 1 - I\left(\dfrac{r - r_1}{r_2 - r_1}\right), & r_1 \leq r \leq r_2, \\ 0, & r_2 \leq r < \infty, \end{cases} \tag{4.3}$$

where r_1 and r_2 are specified constants and where $I(x) = \exp\{-(2x)^{-1}(\ln 2)\exp[(1 - 2x)(1 - x)^{-1}]\}$ is a smooth unit step function on the interval $0 \leq x \leq 1$, having the property $I(0) = 0$, $I(1/2) = 1/2$ and $I(1) = 1$. For $G(s)$ we take

$$G(s) = \frac{1}{2}\begin{cases} 0, & s_3 \leq s \leq s_T, \\ \dfrac{s_1}{s_3 - s_2}\left\{1 + \cos\left[\pi\dfrac{(2s - s_3 - s_2)}{s_3 - s_2}\right]\right\}, & s_2 \leq s \leq s_3, \\ 0, & s_1 \leq s \leq s_2, \\ -\left[1 + \cos\left(\dfrac{\pi s}{s_1}\right)\right], & 0 \leq s \leq s_1, \end{cases} \tag{4.4}$$

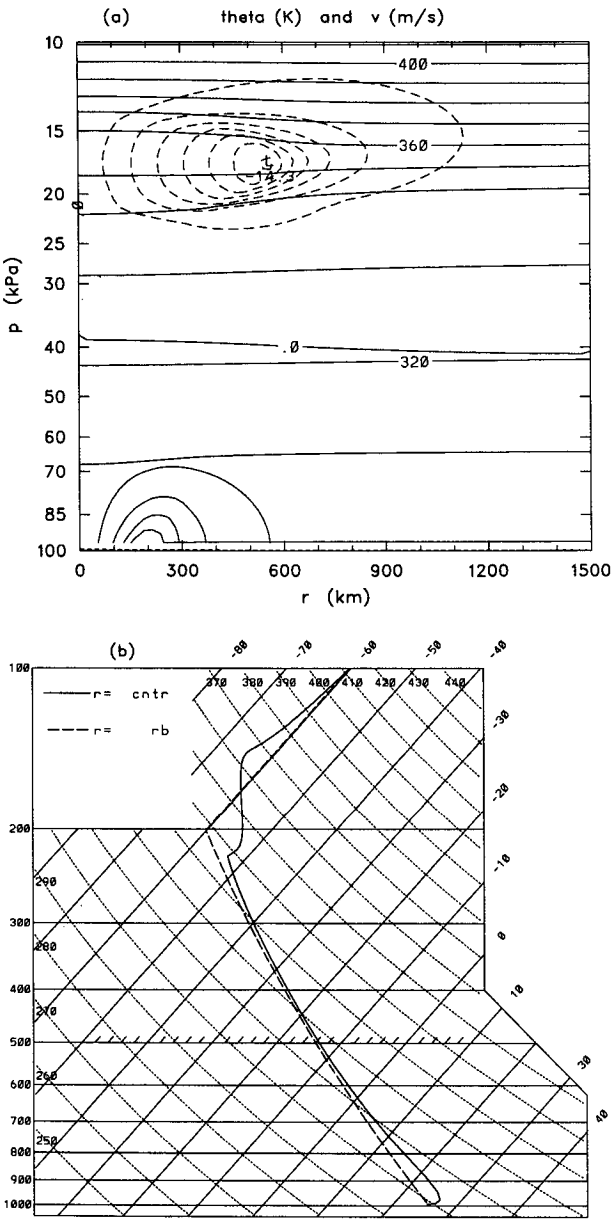

FIG. 4. Results for experiment 1: (a) the nearly horizontal lines are isolines of potential temperature in (r, p) space (10-K contour interval). Also shown are isolines of the tangential wind with the solid wind contours indicating cyclonic flow, and dashed contours anticyclonic flow (2 m s^{-1} contour interval); (b) skew T–log$p$ vertical soundings, with the dashed curve showing the sounding in the far-field environment, and the solid curve the sounding at $r = 0$ in the final adjusted state.

where s_1, s_2, and s_3 are specified constants satisfying $0 < s_1 < s_2 < s_3 \leq s_T$. Thus, for $\hat{\sigma} > 0$, the pseudodensity perturbation has $\sigma' < 0$ in the layer $0 \leq s \leq s_1$, representing a depletion of mass near the earth's surface, and $\sigma' > 0$ in the layer $s_2 \leq s \leq s_3$, representing the injection of that mass in the anvil. This profile is constructed to satisfy $\int_0^{s_T} F(s)ds = 0$, so that mass is simply transferred in the vertical.

We shall now present the results of three experiments. Experiment 1 has a perturbation pseudodensity $\sigma'(r, s)$ obtained from (4.2)–(4.4) using the specified constants $\hat{\sigma} = 3.6$ kg K m^{-3}, $r_1 = 240$ km, $r_2 = 300$ km, $s_1 = c_p \ln(307.9/299.15)$, $s_2 = c_p \ln(337.5/299.15)$, and $s_3 = c_p \ln(366.3/299.15)$. In the basic state, these three entropy surfaces correspond to the isobaric surfaces 700, 200, and 150 mb. In experiment 1 the Coriolis parameter is specified as $f = 2\Omega \sin(30°) = 7.292 \times 10^{-5}$ s^{-1}. In experiment 2, all constants are identical to those in experiment 1, except the Coriolis parameter is specified as $f = 2\Omega \sin(10°) = 2.532 \times 10^{-5}$ s^{-1}. In experiment 3, all constants are identical to those in experiment 1, except the mass injection layer is given by $s_2 = c_p \ln(332.4/299.15)$ and $s_3 = c_p \ln(337.5/299.15)$, which correspond to basic-state pressures of 250 and 200 mb, respectively. Thus, experiment 1 can be considered the control solution, with experiment 2 illustrating the effects of a shift from 30° to 10°N, and with experiment 3 illustrating the effects of shifting the injection region from a 50-mb layer just above the tropopause to a 50-mb layer just below the tropopause. Note that the total mass injected is the same in each experiment.

The results of experiments 1–3 are shown in Figs. 4–6, respectively. In all three experiments, isentropes near the center of the upper-level anticyclone bow apart, giving the isentropes the lens-shaped structure discussed by Gill (1981) in his study of homogeneous intrusions of mass into a rotating stratified fluid. In comparing experiments 1 and 2 we note that the equatorward shift from 30° to 10°N results in a broader and thinner anticyclone, that is, an approximate 50% increase in the radial extent of the anticyclone and an approximate 50% decrease in its vertical depth. This is in rough agreement with the argument that the influence of a potential vorticity anomaly should spread horizontally over a Rossby length and vertically over a Rossby depth. The shift to lower latitudes increases the Rossby length and decreases the Rossby depth.

The final adjusted temperature sounding at $r = 0$ for experiment 1 (Fig. 4b) is similar in certain respects to Bosart and Nielsen's Lake Charles sounding (solid temperature curve in Fig. 3), especially in the upper troposphere and lower stratosphere. Of course, an exact correspondence should not be expected for many reasons, one of which is the probability that the Lake Charles sounding does not represent a final adjusted state. In any event, the warm pool below the anticyclone and the cold pool above the anticyclone, along with the kinked character of the temperature profile, are consistent theoretical and observational features. A notable difference between theory and observation is the relative strengths of the warm and cold pools. The Lake Charles observation (and the Fritsch and Maddox results shown in Figs. 2b,c) indicates that the cold pool

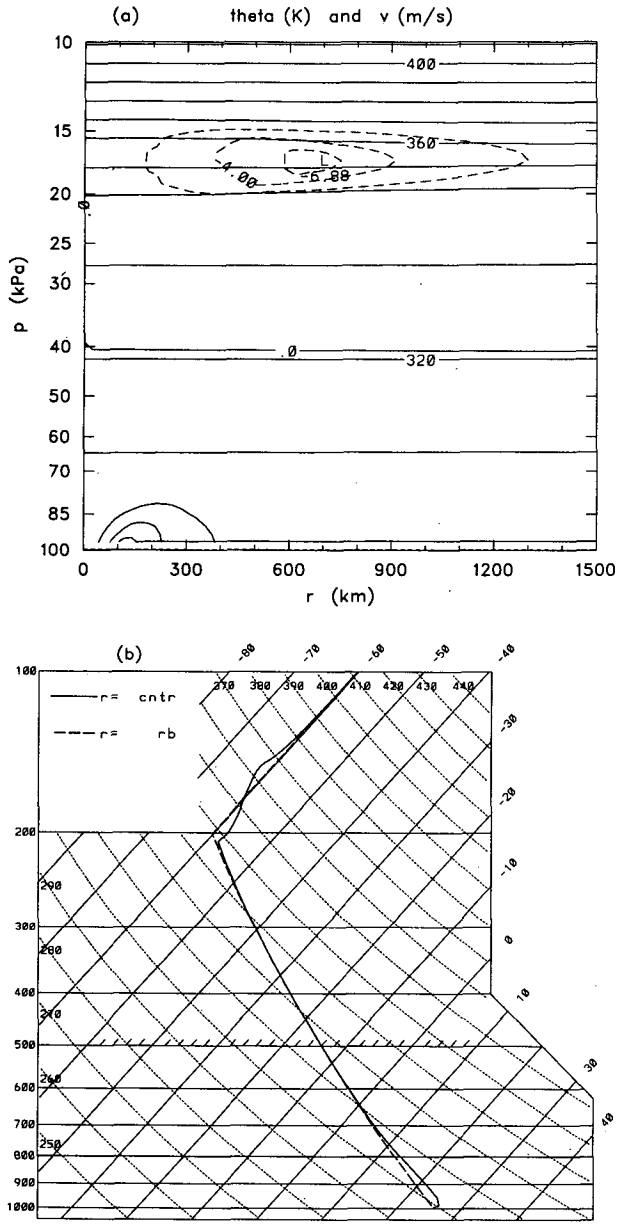

FIG. 5. Results for experiment 2. The only difference from experiment 1 (Fig. 4) is that the latitude of the mesoscale convective system has been shifted from 30° to 10°N. Note that the anticyclonic lens structure is now broader, flatter, and weaker.

is relatively stronger than the warm pool, a feature that does not occur in the theoretical results shown in Fig. 4b. We shall return to this issue in section 5.

In comparing experiments 1 and 3 we note that both experiments result in lower-tropospheric cyclonic flows with maximum tangential winds of 9.9 m s^{-1} at 188-km radius. The differences reside in the anticyclonic flows, with the lower-stratospheric injection (Fig. 4a) resulting in a 14.3 m s^{-1} anticyclonic flow at 562-km radius and the upper-tropospheric injection (Fig. 6a) resulting in a 9.7 m s^{-1} anticyclonic flow at 469-km radius. In both cases the fluid ring lying in the center of the anticyclone originated at a radius of approximately 310 km, but in the stratospheric injection case the radius of this ring has increased by 252 km, while in the tropospheric injection case the radius has increased by only 159 km. In other words, the stronger restoring effect of the stratospheric static stability has resulted in a larger radial displacement of the injected mass and hence produced an anticyclone approxi-

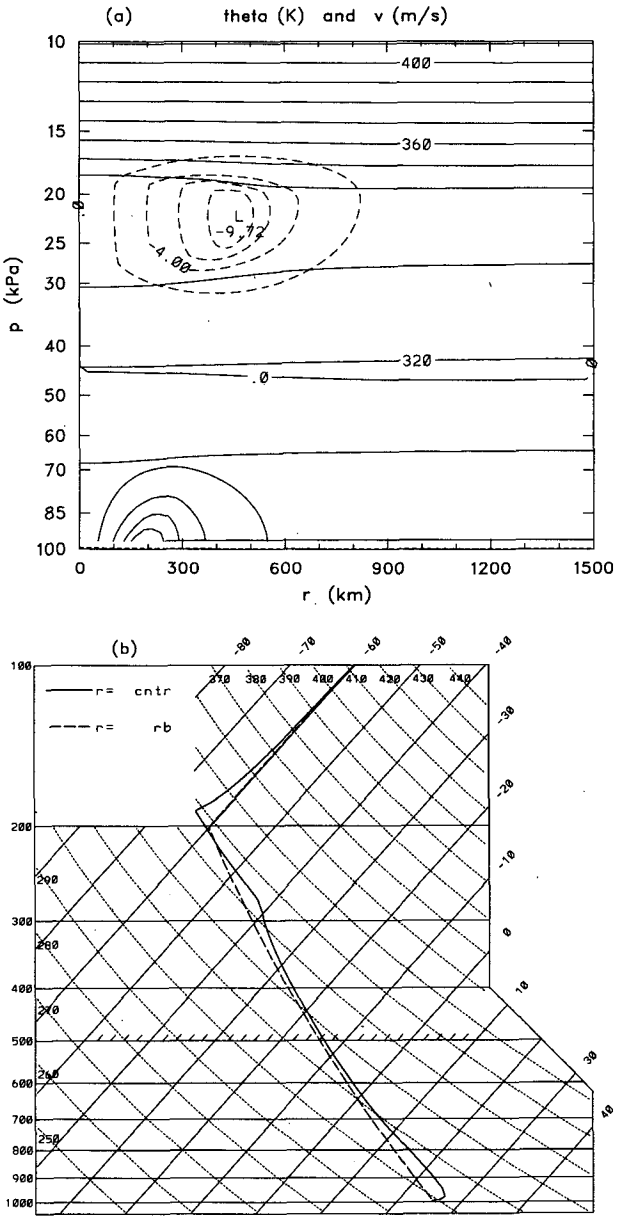

FIG. 6. Results for experiment 3. The only difference from experiment 1 (Fig. 4) is that the level of the mass injection has been shifted from the lower stratosphere to the upper troposphere. Note that the anticyclone is weaker and has a smaller horizontal extent.

mately 50% stronger than in the tropospheric injection case. Thus, the results of experiments 1–3 suggest that for approximately equal mass redistributions the most intense anticyclones will tend to occur at higher latitudes following the outbreak of mesoscale convective systems that inject anvil air into the stable layers of the lower stratosphere.

The nonlinear character of the solutions is illustrated in Fig. 7, which was constructed from a sequence of solutions computed with $\hat{\sigma}$ varying from 0.0 to 3.6 kg K m^{-3}, but with all other constants set to their experiment 1 values. Figure 7 shows how the maximum cyclonic and maximum anticyclonic winds vary with the amount of mass injected into the mesoscale anvil. When this amount is small (e.g., $\hat{\sigma} = 0.5$ kg K m^{-3}), the anticyclone is approximately four times as strong as the cyclone. In contrast, when this amount is large (e.g., $\hat{\sigma} = 3.6$ kg K m^{-3}) the anticyclone is approximately 1.25 times as strong as the cyclone.

5. Effects of the entrainment of stratospheric air by overshooting convective turrets

In experiments 1–3 lower-tropospheric mass was injected into an anvil layer in such a way that the atmosphere above the anvil top was initially undisturbed [i.e., $G(s) = 0$ for $s_3 \leq s \leq s_T$ in (4.4)]. During the adjustment process, an upper-level anticyclone develops, with a warm anomaly below it and a cold anomaly above it. However, the cold anomaly above the anticyclone would probably be stronger if the atmosphere above the anvil top were not initially undisturbed.

While the preponderance of anvil air most certainly comes from the lower troposphere, a small percentage may come from the stratosphere. This stratospheric air is incorporated into the anvil outflow as follows. Parcels moving upward across the tropopause in convective cores often have vertical velocities of 20–40 m s^{-1}. After penetration into the lower stratosphere, buoyancy is rapidly lost as the decelerating convective turret finds itself much colder than the surrounding stratospheric air. As the turret is rapidly decelerated and collapses back downward, warm stratospheric air is entrained, which results in an equilibrium outflow level higher than the original updraft vanishing buoyancy level before stratospheric entrainment. A general rule advanced by Saunders (1962) is that for typical environmental static stability profiles, a visible convective tower advancing upward through the tropopause at 10 m s^{-1} will penetrate 1 km into the stratosphere. Since the maximum vertical parcel velocities inside the convective tower are approximately double the rise rate of the visible tower, a 1-km penetration is associated with maximum updrafts of 20 m s^{-1}, and, by Saunders' arguments, a 2-km penetration is associated with maximum updrafts of 40 m s^{-1}. Penetrations 3 or 4 km into the stratosphere would be expected to be rare. Exactly what percentage of anvil air comes from the stratosphere is not well known, but the basic physical mechanism seems well established through the laboratory work of Saunders (1962), the observational work of Adler and Fenn (1979), Heymsfield and Blackmer (1988), Ebert and Holland (1992), and the theoretical work of Adler and Mack (1986) and Schlesinger (1990). The penetration of convective turrets into the lower stratosphere, the entrainment of warmer stratospheric air, and the production of large anvils above the mean tropopause is also an important aspect of Danielsen's (1982, 1993) stratospheric dehydration mechanism.

In order to explore the effects of the entrainment of stratospheric air by overshooting convective turrets, let us now perform one additional experiment (experiment 4). In this last experiment we specify an impulsive redistribution of mass identical to that defined by (4.1)–(4.4), except that (4.4) is replaced by

$$G(s) = \begin{cases} 0, & s_5 \leq s \leq s_T, \\ \epsilon\hat{G}\left[-1 + I\left(\dfrac{s - s_4}{s_5 - s_4}\right)\right], & s_4 \leq s \leq s_5, \\ \hat{G}\left[1 - (1+\epsilon)I\left(\dfrac{s - s_3}{s_4 - s_3}\right)\right], & s_3 \leq s \leq s_4, \\ \hat{G}I\left(\dfrac{s - s_2}{s_3 - s_2}\right), & s_2 \leq s \leq s_3, \\ 0, & s_1 \leq s \leq s_2, \\ I\left(\dfrac{s}{s_1}\right) - 1, & 0 \leq s \leq s_1, \end{cases} \tag{5.1}$$

where $I(x)$ is the same interpolating function used in (4.3) and where the specified parameters are $s_1 = c_p \ln(307.9/299.15)$, $s_2 = c_p \ln(337.5/299.15)$, $s_3 = c_p \ln(350.4/299.15)$, $s_4 = c_p \ln(366.3/299.15)$, $s_5 = c_p \ln(385.8/299.15)$, $s_T = c_p \ln(411.8/299.15)$, and $\epsilon = 0.1$. The constant $\hat{G}$ is not independently chosen but is related to the other constants by

$$\hat{G} = \frac{s_1(1 - \bar{I})}{(s_3 - s_2)\bar{I} + (s_4 - s_3)[1 - (1+\epsilon)\bar{I}] + \epsilon(s_5 - s_4)(\bar{I} - 1)},$$

where $\bar{I} = \int_0^1 I(x)dx \approx 0.501407$. This choice of $\hat{G}$ guarantees that $\int_0^{s_T} G(s)ds = 0$; that is, mass is simply redistributed. A plot of (5.1) is shown in Fig. 8. The constant ϵ helps determine the amount of stratospheric air entrained into the anvil. For the parameters we have chosen, approximately 91% of the anvil air comes from the lower troposphere, and 9% from the stratosphere just above the anvil. The vertical overshoot implied by Fig. 8 [i.e., the physical depth of the upper region where $G(s) < 0$] is 1.4 km, which is typical of the values observed by Saunders (1962).

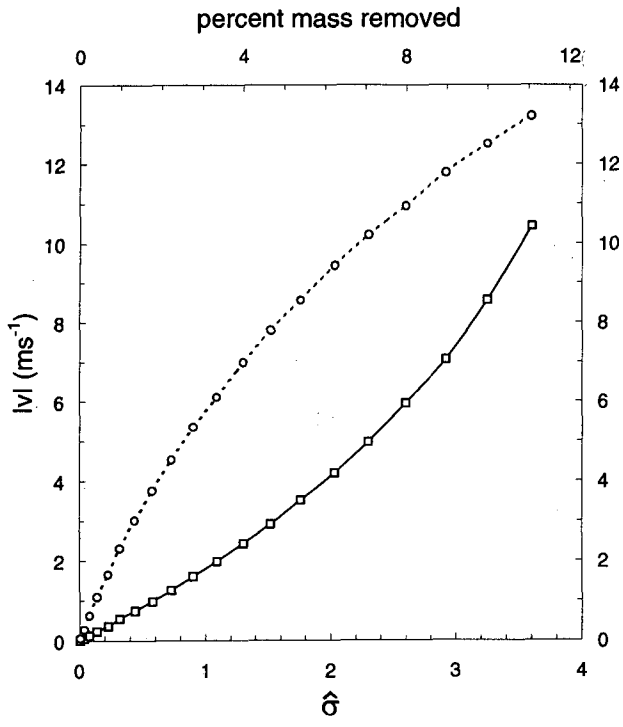

FIG. 7. Maximum anticyclonic flow (dashed line) and maximum cyclonic flow (solid line) as a function of the parameter $\hat{\sigma}$ (kg K m^{-3}). The top scale gives the percentage of mass in the region $0 \leq s \leq s_1$, $0 \leq r \leq 2r_2$, which is removed by the perturbation. The circles mark the actual experiments performed.

As far as the other specified parameters are concerned, experiment 4 is identical to experiment 1, that is, it has the same basic-state pseudodensity $\bar{\sigma}(s)$ used in experiment 1 and has $f = 2\Omega \sin(30°)$, $r_1 = 240$ km, $r_2 = 300$ km, and $\hat{\sigma} = 3.6$ kg K m^{-3}. Note that because of the change of the vertical structure function from (4.4) to (5.1), the total mass injected in experiment 4 is slightly different than in the previous three experiments. This difference need not concern us here since we are focusing our attention on the structural differences caused by stratospheric entrainment.

The results of experiment 4 are shown in Fig. 9. The qualitative effects of the entrainment of stratospheric air can be seen by comparing Fig. 9 with Fig. 4. In comparing Fig. 9a with Fig. 4a, the most obvious difference is in the structure of the upper half of the anticyclone. With stratospheric entrainment, there is larger vertical shear of the tangential wind, resulting in the existence of a weak cyclone above the anticyclone for $r < 300$ km. In comparing Fig. 9b with Fig. 4b, we note that the strength of the cold anomaly at the top of the anvil is stronger when there is stratospheric entrainment. Since the stronger cold anomaly shown in Fig. 9b is more consistent with the observational results shown in Figs. 2b and 2c, we might tentatively conclude that stratospheric entrainment plays a role in determining the detailed structure of the anticyclone. However, this conclusion needs to be confirmed by more detailed simulations that include the effects of radiation and associated convective overturning, both of which may have important influences on the structure of the anticyclone.

6. Concluding remarks

In this paper we have idealized rapid mesoscale convective events as instantaneous mass redistributions. In essence, we have taken the view that a rapidly developing mesoscale convective system represents an occasion when the atmosphere performs a gradient adjustment experiment for us. The approach of treating penetrative convection as a mass source–sink dipole has also been recently used by Shutts (1994), who studied the transient response on a vertically sheared basic state. One of the linear, final adjusted states shown by Shutts (his Fig. 10) is qualitatively similar to the results obtained here.

For the mass redistributions we have considered here, the upper-level anticyclone is always stronger than the lower-level cyclone. While this may be characteristic of the type of mesoscale convective systems studied by Fritsch and Maddox (1981a,b) and Bosart and Nielsen (1993), it is not universal. For example, when the low-level mass is removed from a thicker layer and not injected into such a thin upper layer, the low-level cyclone can become stronger and dominate

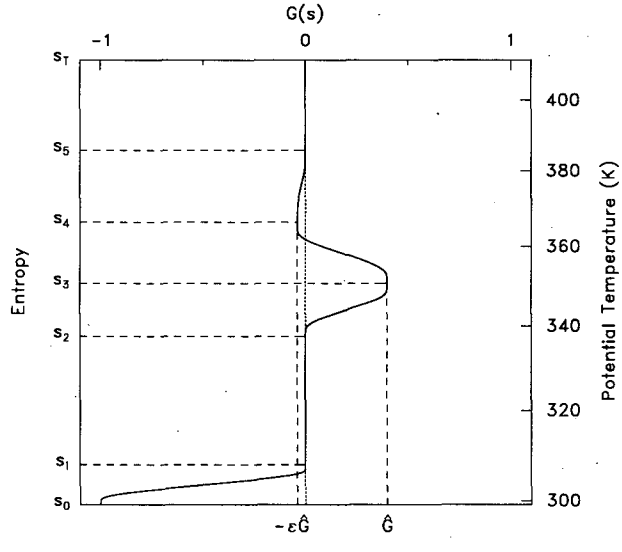

FIG. 8. Vertical profile of $G(s)$ as defined by Eq. (5.1). The region where $G(s) > 0$ is the anvil injection layer. The injected mass comes from the regions where $G(s) < 0$, that is, from the boundary layer and from the stratospheric layer just above the anvil. The profile satisfies the constraint $\int_0^{s_T} G(s)ds = 0$. In the basic-state atmosphere before convective rearrangement, the isentropic levels s_0, s_1, s_2, s_3, s_4, s_5, s_T correspond to the isobaric levels 1000, 700, 200, 175, 150, 125, 100 mb.

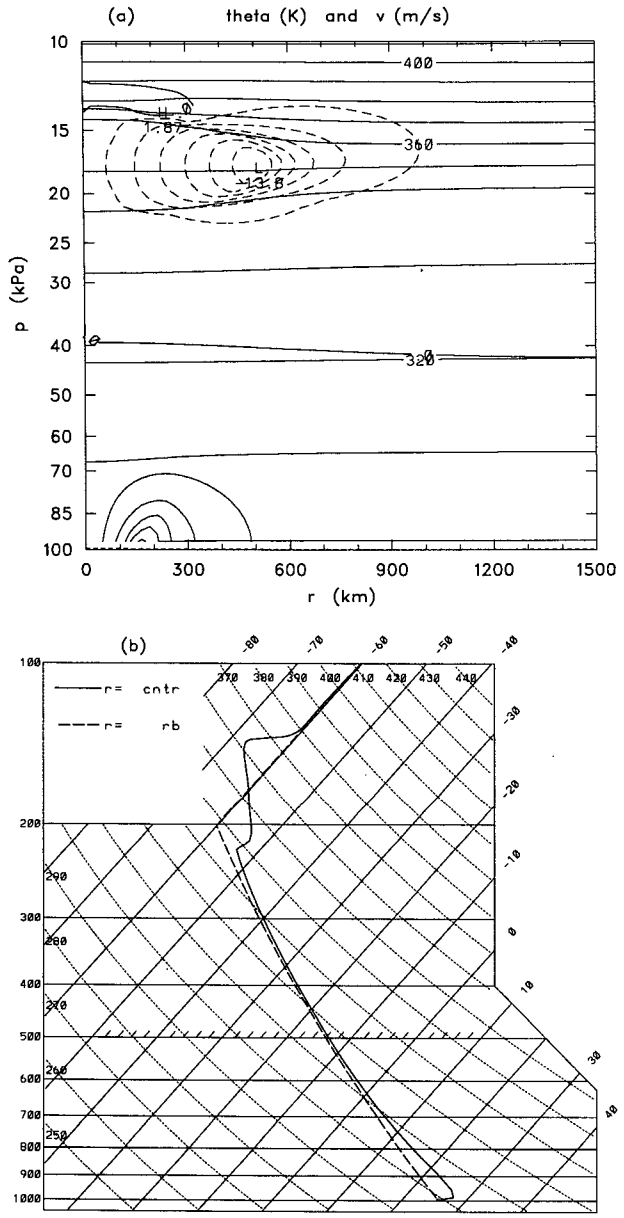

FIG. 9. Results for experiment 4: (a) the nearly horizontal lines are isolines of potential temperature in (r, p) space (10-K contour interval). Also shown are isolines of the tangential wind with the solid wind contours indicating cyclonic flow, and dashed contours anticyclonic flow (2 m s^{-1} contour interval); (b) skew T–log$p$ vertical soundings, with the dashed curve showing the sounding in the far-field environment, and the solid curve the sounding at $r = 0$ in the final adjusted state.

the upper-level anticyclone (Schubert and Alworth 1987).

The analysis presented here could, with slight modifications, be applied to certain oceanographic problems involving penetrative convection, for example, deep ocean convection and hydrothermal venting. The primary modification would be the use of the isopycnic vertical coordinate rather than the isentropic vertical coordinate. Results of such an analysis could then be compared with Helfrich's (1994) extensive laboratory experiments on thermals in fluids with background rotation and stratification.

In closing, we would like to emphasize that the analysis presented here applies to only one of the many physical aspects of convective anvils. In this regard, it is interesting to conjecture on the physical requirements of a detailed, full physics model of cirrus outflow dynamics. The model would need to be nonhydrostatic in order to explicitly simulate the three-dimensional turbulence in the updraft air that is injected into the upper troposphere and lower stratosphere. The model would need to simulate both the downscale energy cascade and the separation of the three-dimensional turbulence into internal gravity waves and quasi-two-dimensional turbulence (Lilly 1988). It would also need to simulate the turbulence generated by differential radiative heating between cirrus cloud base and cloud top. This requires the inclusion of a detailed, coupled treatment of ice physics and radiative transfer, since the differential radiative heating is sensitive to ice water content (Ackerman et al. 1988). The effects of the earth's rotation would be needed to capture that aspect of the dynamics that we have investigated here. Finally, the model would need to simulate the deformation and filamentation of the mesoscale potential vorticity anomaly by the horizontal and vertical shear of the upper-level flow.

Acknowledgments. We are grateful to Glenn Shutts for helpful correspondence and for his careful review of an earlier version of this paper. This work has been supported by the National Science Foundation under Grants ATM-9118966 and ATM-9115485.

APPENDIX

Invertibility Relation at $R = 0$

Since the atmosphere has no physical boundary at $R = 0$, rather than using a boundary condition there we seek an appropriate limiting form of the invertibility relation. To derive this, we start with the average vorticity inside a given radius r, which may be written as

$$\frac{2}{r^2}\int_0^r \zeta r' dr' = f + \frac{2v}{r} = f + \frac{2}{f}\frac{\partial \mathcal{M}}{R\partial R}, \quad \text{(A.1)}$$

where the last step follows from (3.6). Assuming that ζ tends to a finite limit ζ_0 as $r \to 0$, we conclude from (A.1) that $v = O(r)$, which implies from the definition of R that r and R tend to zero together, that is, $R = O(r)$ and $r = O(R)$. Taking the limit of (A.1) as $r \to 0$ yields

$$\zeta_0 = \lim_{R\to 0}\left(f + \frac{2}{f}\frac{\partial \mathcal{M}}{R\partial R}\right). \quad \text{(A.2)}$$

From (3.6) we see that $\lim_{R\to 0}\partial\mathcal{M}/\partial R = 0$, so we can apply L'Hospital's rule to reduce (A.2) to the form

$$\zeta = f + \frac{2}{f}\frac{\partial^2\mathcal{M}}{\partial R^2} \quad \text{at} \quad R = 0. \qquad \text{(A.3)}$$

Now combining the definitions of σ and σ^* yields

$$\frac{\zeta}{f}\sigma^* + \frac{\partial p}{\partial S} = 0, \qquad \text{(A.4)}$$

which upon substituting from (A.3), the ideal gas law, and the hydrostatic relation becomes

$$\left(1 + \frac{2}{f^2}\frac{\partial^2\mathcal{M}}{\partial R^2}\right)\sigma^* + \rho c_p e^{S/c_p}\frac{\partial}{\partial S}\left(e^{-S/c_p}\frac{\partial\mathcal{M}}{\partial S}\right) = 0$$

$$\text{at} \quad R = 0. \qquad \text{(A.5a)}$$

The upper boundary condition (3.8b) applies without change, that is,

$$\frac{\partial\mathcal{M}}{\partial S} = T \quad \text{at} \quad R = 0, \quad S = S_T, \qquad \text{(A.5b)}$$

while the lower boundary condition (3.8c) reduces to

$$\mathcal{M} - c_p\frac{\partial\mathcal{M}}{\partial S} = 0 \quad \text{at} \quad R = 0, \quad S = 0. \qquad \text{(A.5c)}$$

Equations (A.5) constitute the desired invertibility relation at $R = 0$.

REFERENCES

Ackerman, T. P., K.-N. Liou, F. P. J. Valero, and L. Pfister, 1988: Heating rates in tropical anvils. *J. Atmos. Sci.*, **45,** 1606–1623.

Adler, R. F., and D. D. Fenn, 1979: Thunderstorm intensity as determined from satellite data. *J. Appl. Meteor.*, **18,** 502–517.

——, and R. A. Mack, 1986: Thunderstorm cloud top dynamics as inferred from satellite observations and a cloud top parcel model. *J. Atmos. Sci.*, **43,** 1945–1960.

Balsley, B. B., W. L. Ecklund, D. A. Carter, A. C. Riddle, and K. S. Gage, 1988: Average vertical motions in the tropical atmosphere observed by a radar wind profiler on Pohnpei (7°N latitude, 157°E longitude). *J. Atmos. Sci.*, **45,** 396–405.

Bosart, L. F., and J. W. Nielsen, 1993: Radiosonde penetration of an undilute cumulonimbus anvil. *Mon. Wea. Rev.*, **121,** 1688–1702.

Danielsen, E. F., 1982: A dehydration mechanism for the stratosphere. *Geophys. Res. Lett.*, **9,** 605–608.

——, 1993: In situ evidence of rapid, vertical, irreversible transport of lower tropospheric air into the lower tropical stratosphere by convective cloud turrets and by larger-scale upwelling in tropical cyclones. *J. Geophys. Res.*, **98,** 8665–8681.

Ebert, E. E., and G. J. Holland, 1992: Observations of record deep convection in Tropical Cyclone Hilda. *Mon. Wea. Rev.*, **120,** 2240–2251.

Emanuel, K. A., 1989: The finite-amplitude nature of tropical cyclogenesis. *J. Atmos. Sci.*, **46,** 3431–3456.

Fritsch, J. M., and R. A. Maddox, 1981a: Convectively driven mesoscale weather systems aloft. Part I: Observations. *J. Appl. Meteor.*, **20,** 9–19.

——, and ——, 1981b: Convectively driven mesoscale weather systems aloft. Part II: Numerical simulations. *J. Appl. Meteor.*, **20,** 20–26.

Fulton, S. R., 1989: Multigrid solution of the semi-geostrophic invertibility relation. *Mon. Wea. Rev.*, **117,** 2059–2066.

——, and W. H. Schubert, 1980: Geostrophic adjustment in a stratified atmosphere. Atmos. Sci. Pap. 326, Department of Atmospheric Science, Colorado State University, Fort Collins, CO, 97 pp.

Gill, A. E., 1981: Homogeneous intrusions in a rotating stratified fluid. *J. Fluid Mech.*, **103,** 275–295.

Hack, J. J., and W. H. Schubert, 1986: Nonlinear response of atmospheric vortices to heating by organized cumulus convection. *J. Atmos. Sci.*, **43,** 1559–1573.

Helfrich, K. R., 1994: Thermals with background rotation and stratification. *J. Fluid Mech.*, **259,** 265–280.

Heymsfield, G. M., and R. H. Blackmer Jr., 1988: Satellite-observed characteristics of midwest severe thunderstorm anvils. *Mon. Wea. Rev.*, **116,** 2200–2224.

Hoskins, B. J., M. E. McIntyre, and A. W. Robertson, 1985: On the use and significance of isentropic potential vorticity maps. *Quart. J. Roy. Meteor. Soc.*, **111,** 877–946.

Johnson, R. H., W. A. Gallus Jr., and M. D. Vescio, 1990: Near-tropopause vertical motion within the trailing stratiform region of a midlatitude squall line. *J. Atmos. Sci.*, **47,** 2200–2210.

Lilly, D. K., 1988: Cirrus outflow dynamics. *J. Atmos. Sci.*, **45,** 1594–1605.

Maddox, R. A., D. J. Perkey, and J. M. Fritsch, 1981: Evolution of upper tropospheric features during the development of a mesoscale convective complex. *J. Atmos. Sci.*, **38,** 1664–1674.

Saunders, P. M., 1962: Penetrative convection in stably stratified fluids. *Tellus*, **14,** 177–194.

Schlesinger, R. E., 1990: Overshooting thunderstorm cloud top dynamics as approximated by a linear Lagrangian parcel model with analytic exact solutions. *J. Atmos. Sci.*, **47,** 988–998.

Schubert, W. H., and J. J. Hack, 1983: Transformed Eliassen balanced vortex model. *J. Atmos. Sci.*, **40,** 1571–1583.

——, and B. T. Alworth, 1987: Evolution of potential vorticity in tropical cyclones. *Quart. J. Roy. Meteor. Soc.*, **113,** 147–162.

——, J. J. Hack, P. L. Silva Dias, and S. R. Fulton, 1980: Geostrophic adjustment in an axisymmetric vortex. *J. Atmos. Sci.*, **37,** 1464–1484.

Shutts, G. J., 1987: Balanced flow states resulting from penetrative, slantwise convection. *J. Atmos. Sci.*, **44,** 3363–3376.

——, 1994: The adjustment of a rotating, stratified fluid subject to localized sources of mass. *Quart. J. Roy. Meteor. Soc.*, **120,** 361–386.

——, and A. J. Thorpe, 1978: Some aspects of vortices in rotating, stratified fluids. *Pure Appl. Geophys.*, **116,** 993–1006.

——, M. Booth, and J. Norbury, 1988: A geometric model of balanced axisymmetric flows with embedded penetrative convection. *J. Atmos. Sci.*, **45,** 2609–2621.

Thorpe, A. J., 1985: Diagnosis of balanced vortex structure using potential vorticity. *J. Atmos. Sci.*, **42,** 397–406.

——, 1986: Synoptic-scale disturbances with circular symmetry. *Mon. Wea. Rev.*, **114,** 1384–1389.